


Manipulating quantum emission by interface states between a multicomponent moiré lattice and a metasurface

Z. N. Liu, X. Q. Zhao, Y. L. Zhao, S. N. Zhu, and H. Liu 

National Laboratory of Solid State Microstructures, School of Physics,

Collaborative Innovation Center of Advanced Microstructures, Nanjing University, Nanjing 210093, China



(Received 10 April 2023; accepted 22 June 2023; published 7 July 2023)

In recent years, moiré lattice has become a hot topic and has inspired the research upsurge of moiré lattice. In this work, we propose a method of constructing a multicomposite moiré lattice, which is composed of more than three periodic component structures. Moreover, we propose the moiré lattice–metasurface structure, which can realize the multiwavelength interface states between these kinds of moiré lattices and metasurfaces. The wavelength, polarization, and number of moiré interface states can be manipulated flexibly, with anisotropic metasurfaces. These multiwavelength interface states are employed to enhance quantum emission (QE) and over 20 times QE efficiency can be obtained.

DOI: [10.1103/PhysRevA.108.013502](https://doi.org/10.1103/PhysRevA.108.013502)

I. INTRODUCTION

A moiré lattice is a composite structure formed by the overlap of two identical periodic structures [1]. Recently, in the moiré lattice of twisted double-layer graphene, it was found that at the so-called magic angle, the flat band appears near the Fermi level, and introduces nontrivial topological phases [2–4]. Mott insulating phase and superconducting phase are exhibited in the double-layer graphene [5–8]. Meanwhile, the moiré lattice brings the possibility of many other physical phenomena, including moiré excitons [9], fractional Chern insulators [10], natural plasmon photonic crystal [11], etc. Moiré lattices have also introduced interesting physical effects in artificial photonic systems [12,13]. In a two-dimensional moiré lattice, the localization-delocalization transition of light is realized experimentally [14]. The tunable topological transitions and phonon polaritons were achieved in bilayers of α -phase molybdenum trioxide (α -MoO₃) [15,16]. The interlayer quantum coupling in twisted bilayer graphene may be utilized to build various atomically thin metasurfaces [17]. The formations of optical solitons are controlled by the twist angle in moiré lattices [18,19], and magic-angle lasers in nanostructured moiré lattices exhibit salient features [20]. Recently, a coupled-state theory for low-angle twisted bilayer honeycomb photonic lattices reveals a correspondence between fermionic and bosonic moiré systems [21]. Meanwhile, slow light, nonlinear effects, chiral plasmons, thermal emitters, and filters exhibit excellent properties in the moiré lattice system [17,22]. At present, the moiré lattice is formed by the superposition of two periodic structures, while the moiré lattice formed by the superposition of three or more periodic structures is rarely reported.

In this work, a design method of a multicomponent moiré lattice is proposed. We combine three or more periodic

structures to form a very flexible moiré lattice. Meanwhile, a different kind of multiwavelength interface states between the moiré lattice and metal are obtained. The moiré lattice–metal structure can support multiwavelength interface states by designing the structure of the moiré lattice. Furthermore, we can replace the metal layer with a metasurface to manipulate the polarization of the moiré interface states (MISs). In the experiment, this kind of interface state is used to enhance quantum emission (QE). An anisotropic interface state is used to control the polarization of QE.

II. DESIGN OF MOIRÉ LATTICE–METASURFACE STRUCTURE TO REALIZE MOIRÉ INTERFACE STATES

Firstly, let us consider a moiré lattice composed of n photonic crystals with different periods: $\Lambda_1, \Lambda_2, \dots, \Lambda_i \dots \Lambda_n$. The moiré lattice can be expressed as

$$H^n(z) = \sum_{i=1}^n H_{\Lambda_i}(z) \delta_i(z)$$

$$H_{\Lambda_i}(z) = F_{\Lambda_i} \left(\frac{\text{floor}(\frac{z+p_i}{d}) + \text{ceil}(\frac{z+p_i}{d})}{2} d \right), \quad (1)$$

where the function $\text{ceil}(x)$ means the least integer $\geq x$ and the function $\text{floor}(x)$ means the largest nearest $\leq x$. $F_{\Lambda_i}(z) = 1 - 2\text{floor}(\frac{2z}{\Lambda_i}) + 4\text{floor}(\frac{z}{\Lambda_i})$ is a periodic function taking the value 1 or -1 , with a period Λ_i and $\delta_i(z) = \delta[\text{floor}(\frac{z}{d}) - n \text{floor}(\frac{z}{nd}) + 1 - i]$, where $\delta(0) = 1$; otherwise, $\delta = 0$. $H^n(z)$ is the moiré lattice structure function. Where $H^n(z) = 1$, the refractive index equals n_A ; otherwise, n_B . When $\Lambda_1 : \Lambda_2 : \dots : \Lambda_i : \dots : \Lambda_n = q_1 : q_2 : \dots : q_i : \dots : q_n$, where $q_1, q_2, \dots, q_i \dots q_n$ are positive integers, the moiré lattice is periodic, and the period Λ of the moiré lattice is the least common multiple of $\Lambda_1, \Lambda_2, \dots, \Lambda_i \dots \Lambda_n$. It is worth noting that $H_{\Lambda_i}(z)$ is a periodic function with a period Λ_i and can characterize a photonic crystal structure. And the

*liuhui@nju.edu.cn

minimum thickness of the photonic crystals layer $d = \frac{\Lambda_1}{2q_1} = \frac{\Lambda_2}{2q_2} \dots = \frac{\Lambda_i}{2q_i} \dots = \frac{\Lambda_n}{2q_n}$. p_i is a translation constant in the z direction that can be used to tune the reflection phase at the surface of the photonic crystal. Here, we define $z = 0$ as the location of the surface of the photonic crystals.

The interface between the moiré lattice and a metal layer can retain the original interface states between the original photonic crystals and metal layers. Briefly, we can design photonic crystals with different periods depending on the first band gap position. Furthermore, the phase conditions for the existence of interface states at the photonic crystal–metal interface is $\varphi_m + \varphi_{pc} = 0$, where φ_m is the reflection phase of the metal layer surface and φ_{pc} is the reflection phase of the photonic crystal surface [23]. And for the photonic crystal corresponding to $H_{\Lambda_i}(z)$, φ_{pc} can be modulated by p_i . Thus, we can obtain different interface states as we need. In the design, we choose $n_A = 2.17$ and $n_B = 1.46$. Three photonic crystals defined with functions $H_{\Lambda_1}(z)$, $H_{\Lambda_2}(z)$, and $H_{\Lambda_3}(z)$ are taken as instances with $\Lambda_1 = 160$ nm, $\Lambda_2 = 200$ nm, $\Lambda_3 = 240$ nm and $d = 20$ nm. When $p_1 = 40$ nm, $p_2 = 40$ nm, and $p_3 = 40$ nm, the first band gaps of the three photonic crystals are located near 600, 740, and 880 nm, respectively. The interface states between the three photonic crystals and silver layers are obtained at these three wavelengths, respectively. Moreover, according to Eq. (1), we combine the three photonic crystals to form a moiré lattice in Fig. 1(a). In Fig. 1(c), the moiré lattice corresponding to $H^3(z)$ with period $\Lambda = 2d[q_1, q_2, q_3] = 2400$ nm, inherits the band gap of the original photonic crystals (white areas) and in Fig. 1(d), the dark-blue dashed lines are the reflection spectra of the moiré lattice composed of the three photonic crystals. The reflection gaps of the original photonic crystals are also reflection gaps in the spectrum of the moiré lattice (white areas). Furthermore, at $z = 0$, the phase condition for the existence of interface states of photonic crystals–silver still holds for the moiré lattice–silver in Fig. 1(b). The reflection phase of the moiré lattice has three intersection points (red pentagram) with the negative value of the silver reflection phase inside the band gaps. The wavelengths of the three intersection points are 600, 740, and 880 nm. Thus, the wavelengths of the interface states of moiré lattice–silver are 600, 740, and 880, which is shown in the red dashed horizontal lines in Fig. 1(c) and dips in the red line in Fig. 1(d). As shown in Fig. 1(e), we demonstrate the electric field distribution of the three interface states in the moiré lattice–silver structure, which are localized at the interface between the moiré lattice and the silver layer (blue area). Here, we call the interface states between the moiré lattice and a metal layer MISs.

In our moiré lattice–silver structure, the i th MIS can be individually modulated by p_i . The moiré lattice interface is obtained by truncating the lattice and the truncated location is defined as p_i . With p_i increasing, the truncation location of the moiré lattice is shifted to the left. The truncation location affects the reflection phase at the moiré interface. In Fig. 2, the moiré lattice corresponding to $H^3(z)$ is taken as an instance. As shown in Fig. 2(a), when p_1 changes from 0 to 320 nm, the first MIS (dark-blue line) wavelength shifts from 620 to 570 nm significantly. However, the other two MISs' wavelength shifts slightly. As shown in Fig. 2(b), when p_2 changes

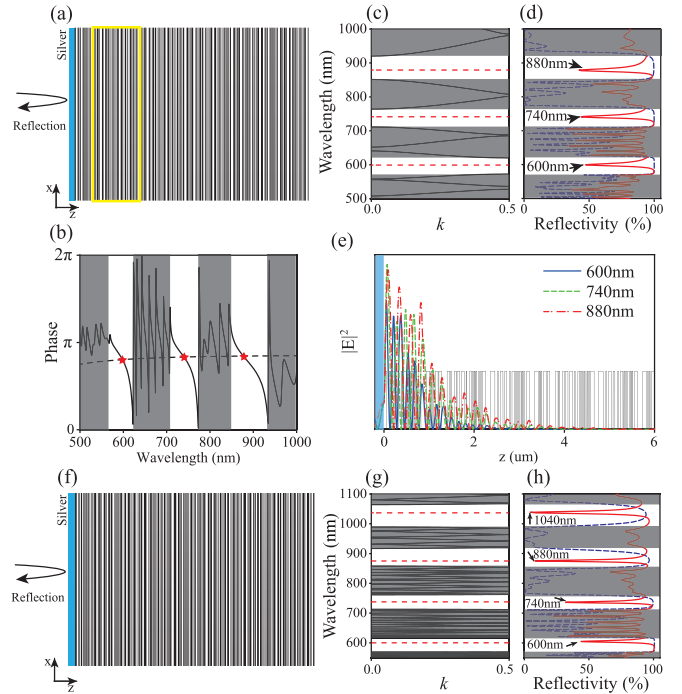


FIG. 1. (a) The moiré lattice–silver structure [the moiré lattice corresponding to $H^3(z)$]. The yellow box is a moiré cell. The curved arrow on the left side is a reflection schematic. (b) The dashed black line represents the calculated negative value of the reflection phase of the silver layer. The black line shows the reflection phase of the moiré lattice. The location of the intersection (red pentagram) of the two lines is MISs. (c) show the band of the moiré lattice and the white regions is the band gaps with the MISs. The red horizontal dashed line is the MISs. (d) The dashed blue line is the reflection spectrum of the moiré lattice and the red line is the reflection spectrum of the moiré lattice–silver structure. (e) Electric field distribution of moiré interface states of 600, 740, and 880 nm, respectively. The blue area is a silver layer. (f) shows moiré lattice–silver structure [the moiré lattice corresponding to $H^4(z)$]. The curved arrow on the left side is a reflection schematic. (g) shows the band of the moiré lattice corresponding to $H^4(z)$ and the white regions are the band gaps. The horizontal dashed red line is the MISs. (h) The dashed blue line is the reflection spectrum of the moiré lattice and the red line is the reflection spectrum of the moiré lattice–silver structure.

from 0 to 400 nm, the second MIS's (green line) wavelength shifts from 770 to 710 nm significantly. However, the other two MISs' wavelength shifts slightly. As shown in Fig. 2(c), when p_3 changes from 0 to 480 nm, the third MIS's (red line) wavelength shifts from 926 to 847 nm significantly. However, the other two MISs' wavelength shifts slightly. The above results show that p_i can be used to individually modulate the i th MIS wavelength. We select the moiré structures (red, green, and blue dots) in Figs. 2(a)–2(c) corresponding to different p_1 , p_2 , and p_3 and plot the reflection phase (red, green, and dark-blue lines) in Figs. 2(d)–2(f). p_i only has a significant effect on the reflection phase modulation of the moiré lattice in the corresponding white region, but a small effect on other regions. This leads to a shift in the wavelength of the i th MIS corresponding to p_i in the moiré lattice–silver structure, as shown in Figs. 2(g)–2(i). In Fig. 2(g), with p_1 increased, the first MIS

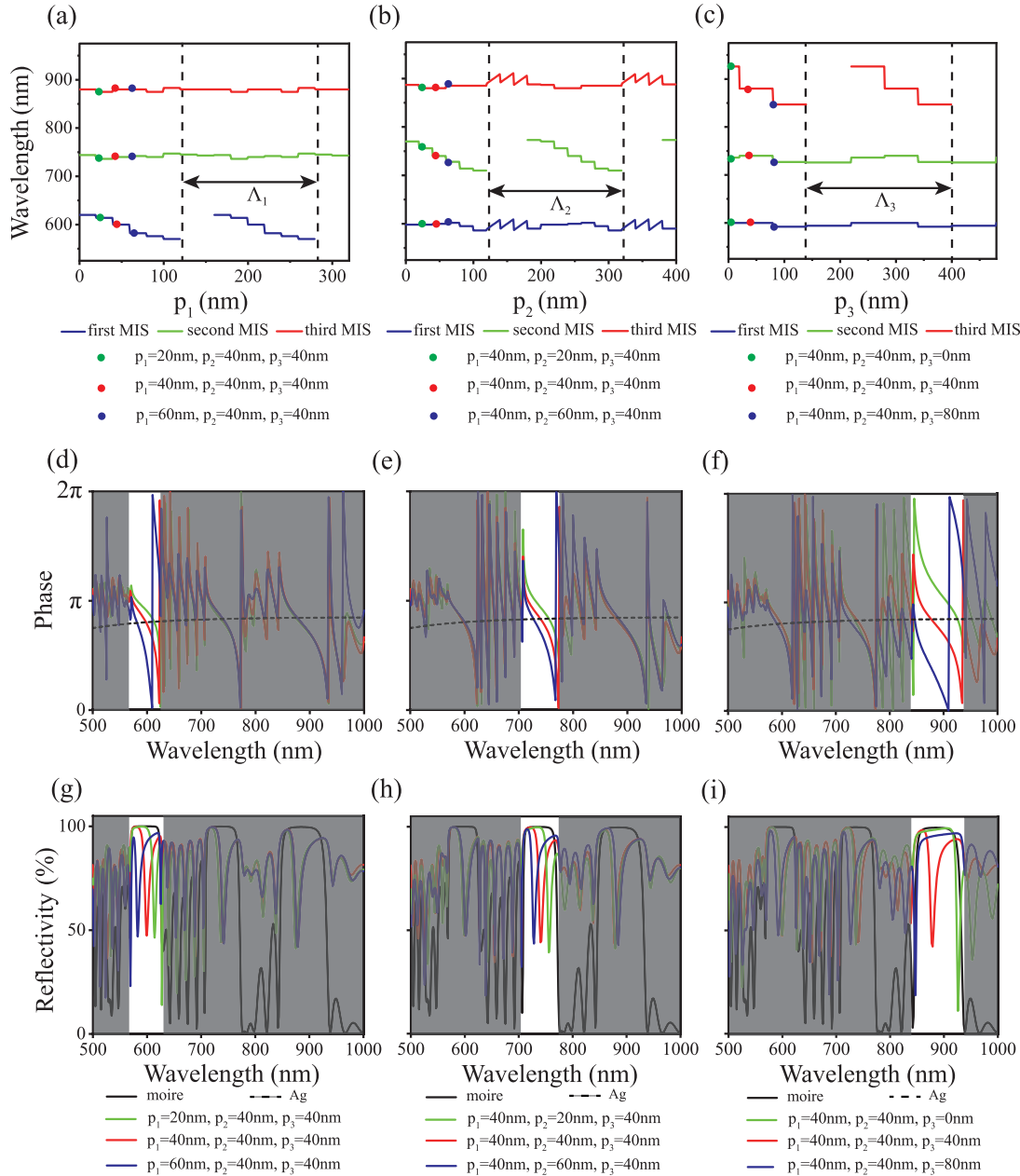


FIG. 2. (a)–(c) show the change in the wavelength of the MISs as p_1 , p_2 , and p_3 change, respectively. (d)–(f) Red, green, and dark-blue lines are the reflection phase of moiré lattice for different p_1 , p_2 , and p_3 cases, respectively, and the black dashed line is the negative of reflection phase of the silver layer. (g)–(i) Reflection spectrum of the corresponding moiré lattice–silver structure. The black line is the reflection spectrum of the moiré lattice corresponding to $H^3(z)$.

(dips in white areas) blueshifts but the other two MISs barely move. In Fig. 2(h), with p_2 increased, the second MIS (dips in white areas) blueshifts but the other two MISs barely move. In Fig. 2(i), with p_3 increased, the third MIS (dips in white areas) blueshifts but the other two MISs barely move. Thus, p_i can be used to individually tune the i th MIS wavelength by controlling the reflection phase of the moiré lattice.

In addition, for the moiré lattices composed of more photonic crystals, the combination rule of the multiwavelength MISs given above is still valid. For instance, we add $H_{\Lambda_4}(z)$ with $\Lambda_4 = 280$ nm to $H^3(z)$ to obtain $H^4(z)$ in Fig. 1(f), and when $p_4 = 300$ nm, the photonic crystal corresponding to $H_{\Lambda_4}(z)$ has interface state with silver at 1040 nm wavelength.

In Fig. 1(g), the moiré lattice corresponding to $H^4(z)$ with period $2d[q_1, q_2, q_3, q_4]$ and $d = 20$ nm, inherits the photonic band gap of the original photonic crystals and the interface states are also retained. As shown in Fig. 1(h), we realize quadruple MISs in the moiré lattice–silver structure. According to Eq. (1), we can achieve more MISs in a moiré lattice–silver structure if more photonic crystals are added.

III. MOIRÉ INTERFACE STATES FOR ENHANCEMENT OF QUANTUM EMISSION

In the above discussion, we find MISs can be obtained at the moiré lattice–silver interface. We can use the

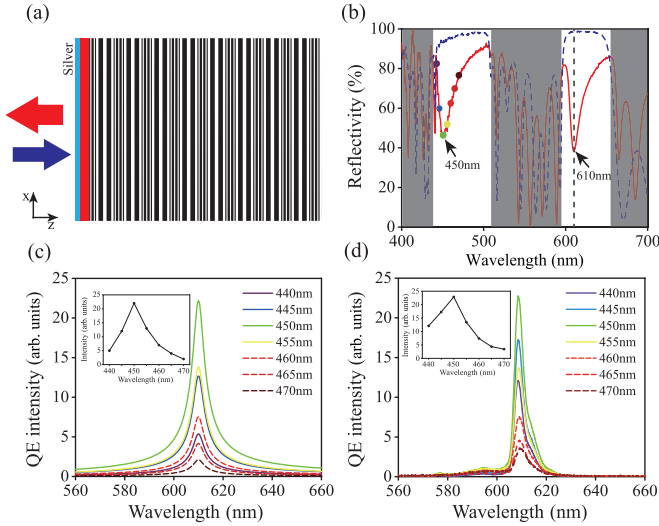


FIG. 3. (a) Schematic diagram of quantum excitation. The dark-blue arrow indicates pump light incident from the silver layer; red arrows indicate QE from the silver layer side. (b) The dotted blue line (red line) is the experimental reflection spectrum of the moiré lattice (moiré lattice–silver structure). The dots correspond to the different pumping laser wavelengths in (c) and (d). (c) The QE intensity with pumping wavelength. (d) The experimental measured QE intensity with pumping wavelength.

multiwavelength interface states to increase the QE efficiency if one MIS is resonant at the pumping wavelength, and the other MIS is resonant at the QE wavelength. Here, we utilized a pump laser with wavelength at 450 nm to excite QE with wavelength at 610 nm. For the photonic crystal, we choose tantalum pentoxide as material A (the refractive index $n_A = 2.17$) and silicon dioxide as material B (the refractive index $n_B = 1.46$). The moiré lattice is designed based on Eq. (1) composed of two periodic components. We choose the parameters $\Lambda_1 = 120$ nm, $\Lambda_2 = 160$ nm and get $d = 20$ nm, $p_1 = 60$ nm, and $p_2 = 20$ nm, which ensure there are two MISs of moiré lattice–silver with wavelength at 450 nm (the first MIS) and 610 nm (the second MIS). The moiré lattice corresponding to $H^2(z)$ is shown in Fig. 3(a). To increase the QE efficiency by moiré lattice, we added a polymethylmethacrylate (PMMA) layer mixed with rare earth (europium), which can be excited by a laser with wavelength shorter than 610 nm and emits fluorescence at 610 nm, on top of the moiré lattice, marked as the red layer in Fig. 3(a). The thickness and the refractive index of the PMMA layer are 160 nm and 1.62, and interface states can be obtained at the interface between the moiré lattice and a silver layer. In Fig. 3(b), the red line is the reflection spectrum of the moiré lattice–silver structure and the dark-blue dashed line is the reflection spectrum of the moiré lattice. The two MISs correspond to the two dips (wavelength at 450 and 610 nm) of the red line. This double-wavelength MIS between the silver layer and the moiré lattice can enhance the pump laser and QE simultaneously, thus increasing the QE efficiency.

To illustrate the enhancement of QE efficiency in the moiré lattice–silver structure, we use a temporal coupled-state theory (see Appendix) [24]. As shown in Fig. 3(c), we give the

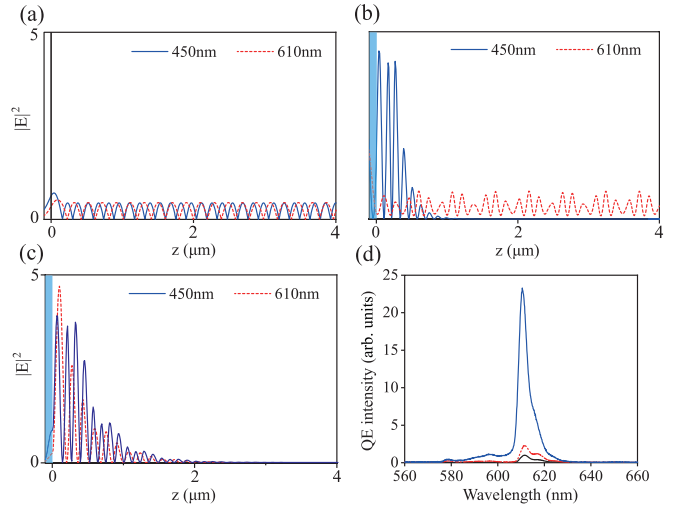


FIG. 4. (a) Electric field distribution of 450 nm (blue line) and 610 nm (dashed red line) of a glass substrate, respectively. The black line is the interface between the glass substrate and the air. (b) Tamm mode distribution of 450 nm (blue line) and electric field distribution of 610 nm (dashed red line). The blue area is silver. (c) Moiré interface modes electric field distribution of 450 nm (blue line) and 610 nm (dashed red line), respectively. The blue area is silver. (d) The blue line is the QE intensity of the moiré lattice–silver structure, the dashed red line is the QE intensity of the original photonic crystal–silver structure, and the black line is the QE intensity of the glass substrate.

calculated Γ (QE intensity) at different pumping wavelengths, which are shown as dots in Fig. 3(b). Clearly, the QE intensity is greatest at the pumping wavelength of 450 nm. As the pumping wavelength is shifted away from the MIS wavelength, the QE intensity is decreased due to the pumping laser departing from the resonance state. The calculation results show that the QE intensity can be dramatically enhanced with MISs. Experimentally, we use a tunable femtosecond laser to excite a quantum emitter (rare earth) in the moiré lattice–silver interface. The pump laser is input on the silver side and the QE intensity is measured on the silver side. As shown in Fig. 3(d), we change the laser wavelength from 440 to 470 nm spaced by 5 nm, keep the power constant, and measure the QE intensity. The QE intensity gets the maximum value at the laser wavelength of 450 nm. The inset shows the peak of QE intensity with different pumping wavelengths, which is in good agreement with the theoretical calculations.

In addition, we compare the QE intensity produced in three different structures: a glass substrate, a Tamm structure, and the moiré lattice–silver structure we mentioned above (corresponding to $H^2(z)$), whose electrical field profiles are given in Figs. 4(a)–4(c). Here, the Tamm structure is defined as a periodic photonic crystal and metal layer, which has a single-wavelength resonance interface state at 450 nm. Usually, Tamm structure shows sharp narrow peak resonance in reflection and transmission spectra. Utilizing this property, optical absorbers, filters, lasers, sensors, etc., can be fabricated. However, the moiré lattice–silver structure not only possesses the resonance properties of Tamm structures but also has no limit on the number of resonance states. No

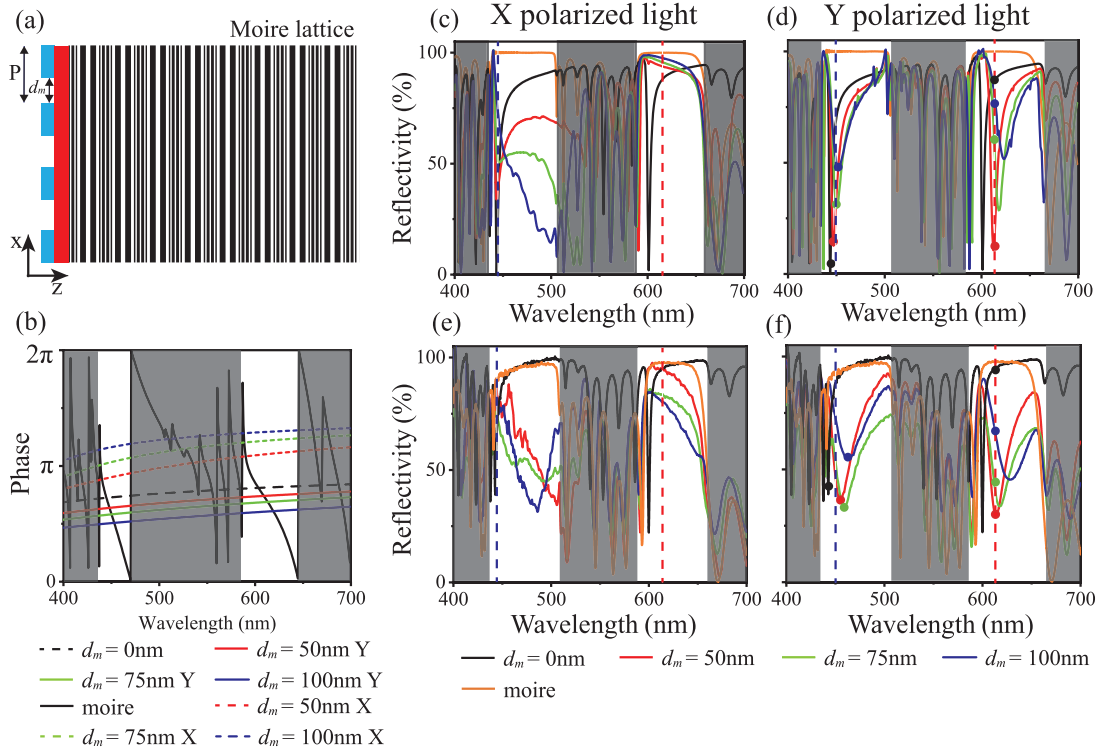


FIG. 5. (a) Moiré lattice–metasurface structure that supports MISs. (b) The solid lines are the calculated negative value of the reflection phase of Y polarized light by the metasurfaces and the dashed lines are the calculated negative value of the reflection phase of X polarized light by the metasurfaces. The black, red, green, and dark-blue lines represent slit widths $d_m = 0$ (equivalent to the silver layer), 50, 75, and 100 nm of the metasurfaces, respectively. The black line shows the reflection phase of light by the moiré lattice. The reflection spectra of the moiré lattice–metasurface structure are shown in (d) and (f) the Y polarized light and in (c) and (e) the X polarized light, where (c),(d), [(e),(f)] are the numerical (experimental) results. The black, red, green, and dark-blue lines represent slit widths $d_m = 0$ (silver layer), 50, 75, and 100 nm, respectively. The orange line represents the reflection spectrum of the moiré lattice. (c)–(f) The white regions are the band gaps we care about. The dashed red lines on the right side, white region are QE wavelength and the dashed blue lines on the left side, white region are selected pumping wavelength in Fig. 6(a). (d),(f) The dots on the right side, white region are leaks of QE for different structures and the dots on the left side, white region are selected pumping wavelength in Fig. 6(c).

field is localized in a substrate without a period in Fig. 4(a). Only one electric field of wavelength 450 nm is localized in Tamm structure in Fig. 4(b). It is worth noting that the moiré lattice supports the resonance interface states at both wavelengths 450 and 610 nm. As shown in Fig. 4(c), in the moiré lattice–silver structure, both the electric fields of two wavelengths are localized at the interface simultaneously. These different electric field distributions affect the coupling coefficient, which affects the QE intensity. To analyze the effect of different structures on QE intensity, we obtained the coupling coefficients in calculations, $|\kappa_2| = 6.62 \times 2\pi$ THz for the moiré lattice–silver structure, $|\kappa_1| = 1.26 \times 2\pi$ THz for the single resonant Tamm structure, and $|\kappa_0| = 0.43 \times 2\pi$ THz for the glass substrate. Since $|\kappa_2| > |\kappa_1| > |\kappa_0|$, the moiré lattice–silver structure has the best QE efficiency. In Ref. [24], the two resonant states are not located at the same locations and are separated by a metal layer. In the structure we can obtain both the resonant states at the same interface between the metal and the moiré lattice, which makes the QE intensity stronger. Experimentally, we use a femtosecond laser with a wavelength of 450 nm to excite the quantum emitters in the three structures with the same incident power. The measured QE intensities are compared in Fig. 4(d). The best QE intensity is produced in the moiré lattice–silver structure, which

is 5 times of the Tamm structure and 20 times of the glass substrate.

IV. METASURFACE MODULATED MOIRÉ INTERFACE STATES

Metasurfaces are two-dimensional artificial nanostructures consisting of periodic subwavelength unit cells. In recent years, the rapid development of metasurfaces bring us many interesting applications, such as beam steering, surface plasmon polariton coupling, metalenses, meta-waveplates, ultrasensitive sensing, biosensors, and dynamical metasurfaces [25,26]. In applications, we expect more flexibility in tuning the MISs, which can be achieved by replacing the metal layer with a metasurface. With the help of the metasurface, the MISs can be manipulated by engineering the reflection phase of the metasurface. With an anisotropic metasurface, we can manipulate the polarization of the MISs. The moiré lattice–metasurface structure is shown schematically in Fig. 5(a). The red area indicates the PMMA layer (150 nm) and the blue part indicates the anisotropic metasurface composed of subwavelength nanoslits. The nanoslits are periodical along the X direction with a thickness of 35 nm and a period $P = 150$ nm. The width of a single slit is d_m , which is a

changed parameter in the designing. We fabricate four samples with different slit widths $d_m = 0$ (silver layer), 50, 75, and 100 nm. The calculated negative value of the reflection phases of X polarized light and Y polarized light by the metasurfaces are shown in Fig. 5(b), respectively. For reference, the calculated reflection phase of the moiré lattice is also shown in Fig. 5(b) as a black solid line. In Fig. 5(b), the dashed lines are the reflection phase of X polarized light, the solid line is the reflection phase of Y polarized light, and the different color lines correspond to the different slit widths of the metasurfaces. The different polarized waves show different changing trends with increasing d_m . As d_m increases, the reflection phase of the X polarized light by the metasurfaces shifts upward but the Y polarized light by the metasurfaces shifts downward. As a result, the intersection points of the reflection phase of the moiré lattice with the negative value of the reflection phases of the different polarized waves by the metasurfaces shift in the opposite direction. This makes the wavelengths of the two different polarized MISs shift in opposite directions. As shown in Figs. 5(c) and 5(d), we calculated the reflection spectra of the different polarized waves by moiré lattice–metasurface structures in simulation, and for reference, the reflection spectrum of moiré lattice (orange line) also is shown. In Fig. 5(c), the wavelengths of the X polarized MISs (dips in white areas) shift to a shorter wavelength and then disappear outside the band gap with increasing d_m . However, in Fig. 5(d), the wavelengths of the Y polarized MISs (dips in white areas) shift to longer wavelengths with increasing d_m . The experimentally measured reflection spectra of different polarized states of the moiré lattice–metasurface structure are shown in Figs. 5(e) and 5(f), which are in good agreement with the simulation results Figs. 5(c) and 5(d), respectively. The above results show that by tuning the metasurface structural parameter d_m , we can flexibly manipulate the resonance wavelength of the different polarized states of MISs.

The above results show that the anisotropic metasurfaces can be used to control the polarization of the interface states. As a result, we can apply the anisotropic metasurfaces to control the polarized states of QE. Here, we still used temporal coupled-state theory to calculate the QE intensities with different polarized states in Fig. 6(a). In Fig. 6(a), the red line is the X polarized QE intensity with $d_m = 50$ nm and the pumping wavelength is 445 nm. The blue line is the Y polarized QE intensity with $d_m = 50$ nm and the pumping wavelength is 450 nm. It can be seen that the Y polarized QE intensity is nearly three times that of the X polarized QE intensity. This is because both the Y polarized pumping (blue dashed vertical line) and the QE wavelengths (red dashed vertical line) are at the MISs wavelength positions, as shown in Fig. 5(d). However, the X polarized QE wavelength (red dashed vertical line) is not at the MIS wavelength position, as shown in Fig. 5(c). In Fig. 6(b), we use a 450-nm femtosecond laser to excite a quantum emitter in the moiré lattice–metasurface structure and then the Y polarized QE intensity is measured on the metasurface side (blue line). Then, we use a 445-nm femtosecond laser with the same incident power to excite a quantum emitter in the moiré lattice–metasurface structure, and then the X polarized QE intensity is measured on the metasurface side (red dashed line). The experimentally measured results in Fig. 6(b) are in good agreement with the

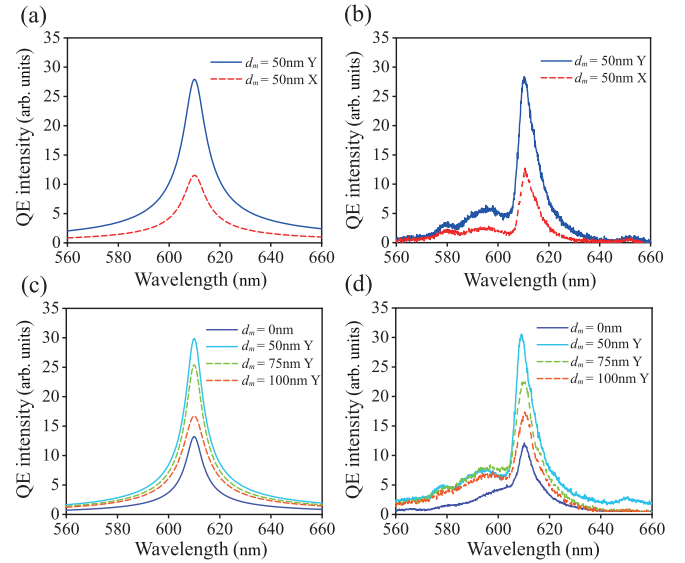


FIG. 6. (a) The QE intensity with different polarized states in the moiré lattice–metasurface structure with $d_m = 50$ nm. (b) The experimental measured QE intensity with different polarized states in the moiré lattice–metasurface structure with $d_m = 50$ nm. (c) The Y polarized QE intensity with different d_m in the moiré lattice–metasurface structure. The pumping wavelengths correspond to the dots on the left side, white region in Fig. 5(d). (d) The experimental measured Y polarized QE intensity with different d_m in the moiré lattice–metasurface structure. The pumping wavelengths correspond to the dots on the left side, white region in Fig. 5(f).

theory in Fig. 6(a). The above results show the metasurfaces can modulate not only the polarized state of QE but also the QE intensity. In Fig. 6(c), we used temporal coupled-state theory to calculate the Y polarized QE intensity in the different moiré lattice–metasurface structures with slit widths ($d_m = 0, 50, 75, 100$ nm). The pumping wavelengths are shown as the black, red, green, and dark-blue dots (left side, white area) for different moiré lattice–metasurface structures with slit widths ($d_m = 0, 50, 75, 100$ nm) in Fig. 5(d), respectively. The QE wavelength positions are shown in the red dashed line and the reflectivity (QE wavelength) corresponding moiré lattice–metasurface structures ($d_m = 0, 50, 75, 100$ nm) are shown as the black, red, green, and dark-blue dots in the second gap in Fig. 5(d), respectively. In Fig. 6(c), the comparison between the QE intensity of different samples is decreased from the best to the worst as $d_m = 50, 75, 100$, and 0 nm. This is because the change of d_m shifts the wavelength of the MISs to depart away from the QE wavelength (610 nm). In Fig. 6(d), we use a tunable femtosecond laser to excite a quantum emitter in the moiré lattice–metasurface structures to produce QE. For different samples, we choose different pumping wavelengths to excite the quantum emitter, which is shown as the black, red, green, and dark-blue dots on the left in Fig. 5(f). Keeping the incident power unchanged, we measure the Y polarized QE intensity of different moiré lattice–metasurface structures. The experimentally measured results in Fig. 6(d) are in good agreement with the theoretical calculations in Fig. 6(c). The above results show that by tuning the metasurface, we can manipulate the polarization state and intensity of the QE.

V. CONCLUSION AND DISCUSSION

In conclusion, we propose a method of constructing a multicomponent moiré lattice. The moiré lattice–metasurface structure can support multiwavelength MISs, of which the wavelength, polarization, and number can be manipulated flexibly. Furthermore, based on the MISs we propose a feasible method to realize the metasurface modulate the polarized state of QE, which can be generalized to nonlinear optics or other light-matter interaction processes with multiwavelength waves. We believe that the designing method of constructing multicomponent moiré lattice and the MISs can be extended to other kinds of moiré physical systems in the future. Some other special interesting applications are possible to obtain, such as optical detection devices, filters, and sensors.

ACKNOWLEDGMENT

This work was financially supported by the National Natural Science Foundation of China (Grants No. 92163216, No. 92150302, and No. 62288101).

APPENDIX: TEMPORAL COUPLED MODE THEORY FOR MANIPULATING QUANTUM EMISSION BY MOIRÉ INTERFACE STATES

To explain the MIS structure enhanced quantum emission efficiency, we used temporal coupled mode theory. In this theory, first MIS and second MIS respectively refer to cavity modes 1 and 2, which are described as a kind of resonance with amplitude $A = [a, b]^T$. Among them, the first MIS corresponds to the higher frequency mode, which refers to the pump laser, and the second MIS corresponds to the lower frequency mode, which is the emission wavelength of quantum emitters. Due to the quantum emitter with a two-energy system, it enables the coupling of two orthogonal cavity modes with different frequencies. In addition, the internal leap process of quantum emitters is unidirectional, so it can be excited by photons of higher frequencies and converted into photons of lower frequencies, but the inverse condition is not allowed. Therefore, we deem that the coupling of the first MIS and the second MIS cavities is unidirectional, that is, the first MIS cavity can couple to the second MIS cavity, while the second MIS cavity cannot couple in turn. The first MIS cavity in our structure is driven by an applied pump laser, while the second MIS cavity is excited by coupling between the two cavities

through quantum emitters. And the coupling equations are

$$\begin{aligned} \frac{da}{dt} &= (j\omega_a - \gamma_1)a + S_+, \\ \frac{db}{dt} &= (j\omega_b - \gamma_2)b + \kappa a, \end{aligned} \quad (\text{A1})$$

where ω_a (ω_b) is the eigenfrequency of the first MIS (second MIS). S_+ is the intensity of interaction between the first MIS cavity and the outside environment. γ_1 (γ_2) is the attenuation rate from the radiative damping and can be expressed in terms of the full width at half maximum of resonant wavelength. κ represents the coupling coefficient between the two cavities, which is directly proportional to the overlapping integral of the electric field:

$$\kappa = \frac{(\varepsilon_0 - \varepsilon_{\text{PMMA}})\omega_0 \int_{\text{PMMA}} d\mathbf{r}^3 \mathbf{E}_1^* \cdot \mathbf{E}_2}{\langle \phi_1 | \phi_1 \rangle},$$

$$\langle \phi_{1(2)} | \phi_{1(2)} \rangle = \sum_{m \in \text{all}} \int_m d\mathbf{r}^3 (\varepsilon_m \mathbf{E}_{1(2)}^* \cdot \mathbf{E}_{1(2)} + \mu_m \mathbf{H}_{1(2)}^* \cdot \mathbf{H}_{1(2)}), \quad (\text{A2})$$

where ε_0 and ε_m are the absolute permittivity for the vacuum and the materials, respectively. μ_0 and μ_m are, respectively, the permeability of the vacuum and the materials. $\mathbf{E}_{1(2)}$ and $\mathbf{H}_{1(2)}$ are, respectively, the electric and magnetic field distribution of resonant modes. Here, we use the normalized electric field, i.e., $\langle \phi_1 | \phi_1 \rangle = \langle \phi_2 | \phi_2 \rangle$.

In our structure, the second MIS cavity is coupled with the wavelength of the quantum emitter embedded in a moiré lattice–metal configuration. The leakage of the second MIS cavity is expressed as $\Gamma = |\gamma_2 b|$. To simplify the model, we consider the interaction strength of the first MIS cavity with the pump laser as constant 1, then we can obtain the emission amplitude $\Gamma = \frac{\kappa \gamma_2 S_+}{\sqrt{[(\omega_l - \omega_a)^2 + \gamma_1^2][(\omega - \omega_b)^2 + \gamma_2^2]}}$, where ω_l indicates the frequency of the pump laser. Clearly, the quantum emission intensity Γ is affected by the pump laser frequency ω_l and the coupling strength κ . As shown in Fig. 3(c), we calculated the quantum emission intensity Γ at different frequencies of the pump laser ω_l . The inset shows the peak intensity of quantum emission at different laser wavelengths. Clearly, the quantum emission intensity is greatest at the pump laser wavelength of 450 nm and coupling coefficient $|\kappa_2| = 6.62 \times 2\pi$ THz. The calculation results show that the quantum emission intensity can be greatly improved in the moiré interface state structure.

- [1] O. Kafri and I. Glatt, *The Physics of Moire Metrology* (Wiley, New York, 1990).
- [2] R. Bistritzer and A. H. MacDonald, Moiré bands in twisted double-layer graphene, *Proc. Natl. Acad. Sci. USA* **108**, 12233 (2011).
- [3] Z. Song, Z. Wang, W. Shi, G. Li, C. Fang, and B. A. Bernevig, All Magic Angles in Twisted Bilayer Graphene are Topological, *Phys. Rev. Lett.* **123**, 036401 (2019).
- [4] G. Tarnopolsky, A. J. Kruchkov, and A. Vishwanath, Origin of Magic Angles in Twisted Bilayer Graphene, *Phys. Rev. Lett.* **122**, 106405 (2019).

- [5] Y. Cao, V. Fatemi, A. Demir, S. Fang, S. L. Tomarken, J. Y. Luo, J. D. Sanchez-Yamagishi, K. Watanabe, T. Taniguchi, E. Kaxiras *et al.*, Correlated insulator behaviour at half-filling in magic-angle graphene superlattices, *Nature (London)* **556**, 80 (2018).
- [6] H. S. Arora, R. Polski, Y. Zhang, A. Thomson, Y. Choi, H. Kim, Z. Lin, I. Z. Wilson, X. Xu, J. H. Chu *et al.*, Superconductivity in metallic twisted bilayer graphene stabilized by WSe₂, *Nature (London)* **583**, 379 (2020).
- [7] P. Stepanov, I. Das, X. Lu, A. Fahimniya, K. Watanabe, T. Taniguchi, F. H. L. Koppens, J. Lischner, L. Levitov, and D. K.

- Efetov, Untying the insulating and superconducting orders in magic-angle graphene, *Nature (London)* **583**, 375 (2020).
- [8] S. Wu, Z. Zhang, K. Watanabe, T. Taniguchi, and E. Y. Andrei, Chern insulators, van Hove singularities and topological flat bands in magic-angle twisted bilayer graphene, *Nat. Mater.* **20**, 488 (2021).
- [9] K. Tran, G. Moody, F. Wu, X. Lu, J. Choi, K. Kim, A. Rai, D. A. Sanchez, J. Quan, A. Singh *et al.*, Evidence for moiré excitons in van der Waals heterostructures, *Nature (London)* **567**, 71 (2019).
- [10] A. Abouelkomsan, Z. Liu, and E. J. Bergholtz, Particle-Hole Duality, Emergent Fermi Liquids, and Fractional Chern Insulators in Moiré Flatbands, *Phys. Rev. Lett.* **124**, 106803 (2020).
- [11] S. S. Sunku, G. X. Ni, B. Y. Jiang, H. Yoo, A. Sternbach, A. S. McLeod, T. Stauber, L. Xiong, T. Taniguchi, K. Watanabe *et al.*, Photonic crystals for nano-light in moiré graphene superlattices, *Science* **362**, 1153 (2018).
- [12] J. B. Khurgin, Light slowing down in Moiré fiber gratings and its implications for nonlinear optics, *Phys. Rev. A* **62**, 013821 (2000).
- [13] A. Kocabas, S. S. Senlik, and A. Aydinli, Slowing Down Surface Plasmons on a Moiré Surface, *Phys. Rev. Lett.* **102**, 063901 (2009).
- [14] P. Wang, Y. Zheng, X. Chen, C. Huang, Y. V. Kartashov, L. Torner, V. V. Konotop, and F. Ye, Localization and delocalization of light in photonic moiré lattices, *Nature (London)* **577**, 42 (2020).
- [15] M. Chen, X. Lin, T. H. Dinh, Z. Zheng, J. Shen, Q. Ma, H. Chen, P. Jarillo-Herrero, and S. Dai, Configurable phonon polaritons in twisted α -MoO₃, *Nat. Mater.* **19**, 1307 (2020).
- [16] G. Hu, Q. Ou, G. Si, Y. Wu, J. Wu, Z. Dai, A. Krasnok, Y. Mazar, Q. Zhang, Q. Bao *et al.*, Topological polaritons and photonic magic angles in twisted α -MoO₃ bilayers, *Nature (London)* **582**, 209 (2020).
- [17] X. Lin, Z. Liu, T. Stauber, G. Gomez-Santos, F. Gao, H. Chen, B. Zhang, and T. Low, Chiral Plasmons with Twisted Atomic Bilayers, *Phys. Rev. Lett.* **125**, 077401 (2020).
- [18] Q. Fu, P. Wang, C. Huang, Y. V. Kartashov, L. Torner, V. V. Konotop, and F. Ye, Optical soliton formation controlled by angle twisting in photonic moiré lattices, *Nat. Photon.* **14**, 663 (2020).
- [19] Y. V. Kartashov, F. Ye, V. V. Konotop, and L. Torner, Multifrequency Solitons in Commensurate-Incommensurate Photonic Moiré Lattices, *Phys. Rev. Lett.* **127**, 163902 (2021).
- [20] X. R. Mao, Z. K. Shao, H. Y. Luan, S. L. Wang, and R. M. Ma, Magic-angle lasers in nanostructured moiré superlattice, *Nat. Nanotechnol.* **16**, 1099 (2021).
- [21] K. Dong, T. Zhang, J. Li, Q. Wang, F. Yang, Y. Rho, D. Wang, C. P. Grigoropoulos, J. Wu, and J. Yao, Flat Bands in Magic-Angle Bilayer Photonic Crystals at Small Twists, *Phys. Rev. Lett.* **126**, 223601 (2021).
- [22] B. Lou, N. Zhao, M. Minkov, C. Guo, M. Orenstein, and S. Fan, Theory for Twisted Bilayer Photonic Crystal Slabs, *Phys. Rev. Lett.* **126**, 136101 (2021).
- [23] M. Xiao, Z. Q. Zhang, and C. T. Chan, Surface Impedance and Bulk Band Geometric Phases in One-Dimensional Systems, *Phys. Rev. X* **4**, 021017 (2014).
- [24] C. Xu, C. Sheng, S. Zhu, and H. Liu, Enhanced directional quantum emission by tunable topological doubly resonant cavities, *Opt. Express* **29**, 16727 (2021).
- [25] Z. P. Li, G. T. Cao, C. H. Li, S. H. Dong, Y. Deng, X. K. Liu, J. S. Ho, and C. W. Qiu, Non-Hermitian electromagnetic metasurfaces at exceptional points, *Prog. Electromagn. Res.* **171**, 1 (2021).
- [26] F. Ding, A review of multifunctional optical gap-surface plasmon metasurfaces, *Prog. Electromagn. Res.* **174**, 55 (2022).